

Article

# Dissolution of $M_{23}C_6$ and New Phase Re-Precipitation in Fe Ion-Irradiated RAFM Steel

Zheng Yang <sup>1</sup>, Shuoxue Jin <sup>2,\*</sup> , Ligang Song <sup>2</sup>, Weiping Zhang <sup>1</sup>, Li You <sup>3</sup> and Liping Guo <sup>1,\*</sup>

<sup>1</sup> Hubei Key Laboratory of Nuclear Solid Physics, Key Laboratory of Artificial Micro- and Nano-Structures of Ministry of Education and School of Physics and Technology, Wuhan University, Wuhan 430072, China; yangzheng34@msn.com (Z.Y.); zhangweiping@whu.edu.cn (W.Z.)

<sup>2</sup> Multi-Discipline Research Center, Institute of High Energy Physics, Chinese Academy of Sciences, Beijing 100049, China; songlg@ihep.ac.cn

<sup>3</sup> Key Laboratory for Advanced Metals and Materials, University of Science and Technology Beijing, Beijing 100083, China; youli-0104321@163.com

\* Correspondence: jinshuoxue@ihep.ac.cn (S.J.); guolp@whu.edu.cn (L.G.);  
Tel.: +86-10-8823-5971 (S.J.); +86-27-6875-2481 (ext. 2223) (L.G.)

Received: 16 April 2018; Accepted: 12 May 2018; Published: 14 May 2018



**Abstract:** The  $M_{23}C_6$  precipitate plays a major role in preventing the sliding of the grain boundary and strengthens the matrix in the reduced-activation ferritic/martensitic (RAFM) steel. However, its stability might be reduced under irradiation. The microstructural instability of the  $M_{23}C_6$  precipitates in the RAFM steels irradiated at 300 °C with Fe ions up to a peak dose of 40 dpa was investigated by transmission electron microscopy. A “Core/Shell” morphology was found for the pre-existing  $M_{23}C_6$  and a large number of new small phases appeared in parallel near the periphery of the precipitates after irradiation. The loss of crystallinity of the  $M_{23}C_6$  periphery due to the dissolution of carbon atoms into the interface (C-rich “Shell”) actually decreased the size of the Cr-rich “Core”. The new phase that formed around the pre-existing precipitates was  $M_6C$  ( $Fe_3W_3C$ ), which was formed through the carbide transformation of  $M_{23}C_6$  to  $M_6C$ .

**Keywords:**  $M_{23}C_6$ ; ion irradiation;  $M_6C$ ; amorphization; RAFM steels

## 1. Introduction

Reduced-activation ferritic/martensitic (RAFM) steels have excellent mechanical strength, low thermal expansion coefficient, high thermal conductivity and good resistance to radiation-induced swelling and helium embrittlement [1–4]. Thus, they have potential uses in new-generation fission reactors and future fusion reactors [5]. It is well known that several typical RAFM steels can be used for test blanket modules in the International Thermonuclear Experimental Reactor [6], which includes Eurofer97, 9Cr2WVTa and China Low Activation Martensitic (CLAM) steels. These RAFM steels undergo various transformation processes, including transformation of the ferritic steel structure (body centered cubic) to a martensitic steel structure (body centered tetragonal) after quenching. The  $M_{23}C_6$  (Cr-rich carbide) precipitate preferentially forms at the martensitic lath and grain boundaries after thermal treatment. The  $M_{23}C_6$  phase is very stable at temperatures below 820 °C [7], which plays a critical role in retaining the physical and mechanical properties of RAFM steels at elevated temperatures [6]. This prevents the grain boundary sliding [8] and strengthens the matrix by exerting a large Zener pinning force on the martensitic lath boundaries compared to the MX phase in RAFM steels [7,9]. However, under thermal, stress and irradiation conditions, the precipitate stability may be reduced [10–12]. Irradiation can increase the diffusion rates due to the production of point defects. The interface between the second-phase particle and the matrix was shown to function as a sink that

traps point defects. It is reported that the interface is an important factor in element segregation and swelling behaviors due to the trapping of gas atoms and point defects [9,13,14]. The size of the  $M_{23}C_6$  precipitates increases in the 9Cr-2WV steels during neutron irradiation [15] and CLAM steel after H and D ion irradiation [16]. The irradiation-induced amorphous transformation of  $M_{23}C_6$  precipitates was observed in 800-MeV proton irradiated martensitic steels [17–19] and in 9Cr-1Mo ferritic/martensitic steel irradiated with 0.5 dpa at low temperatures [20]. The changes in the specimen microstructure, such as the secondary phases/precipitates induced by irradiation, will affect mechanical properties, including fracture toughness [21]. Therefore, examining and understanding the mechanism of  $M_{23}C_6$  phase instabilities under irradiation is essential in evaluating the response of  $M_{23}C_6$  against irradiation, which is also an essential part of developing radiation-resistant RAFM steels.

In this work, we investigate the microstructural instability of  $M_{23}C_6$  precipitates in the RAFM steels due to irradiation. The mechanism of dissolution and re-precipitation will be discussed.

## 2. Experimental

### 2.1. Material Preparation

The chemical compositions of the RAFM steel test materials are shown in Table 1. The bulk specimens underwent heat treatment as follows: quenching at 1000 °C for 40 min and water cooled, before being tempered at 740 °C for 2 h and air cooled. A disc-like specimen with a diameter of 3 mm was punched out from a ~0.1 mm thick sample cut from the bulk RAFM steel and thinned to its final thickness. The standard TEM specimens were prepared by the conventional jet electropolishing methods using 5% perchloric acid and 95% ethanol polishing solution at −30 °C.

**Table 1.** Chemical compositions of Reduced-activation ferritic/martensitic (RAFM) steel in wt. %.

Fe	C	Cr	W	V	Mn	Si	P	S
Bal.	0.088	9.24	2.29	0.25	0.49	0.25	0.0059	0.001

### 2.2. Irradiation Experiments

The irradiation experiments were carried out in the Accelerator Laboratory of Wuhan University and the samples were irradiated to a peak dose of 40 dpa with 100-keV Fe ion at 300 °C. The damage profile calculated by the Stopping and Range of Ions in Materials (SRIM) code simulation is shown in Figure 1, where the displacement energy was  $E_d = 40$  eV. A uniform ion beam current (~1  $\mu$ A) was created for holding by scanning in both the horizontal and vertical directions. The sample temperature was monitored with a thermocouple throughout the irradiation process, which touched the implantation surface of the sample. The microstructure analysis and composition measurements were conducted with a field-emission-gun analytical Tecnai G2 F30 microscope (Beijing, China), which had a nominal spot size of 0.5 nm, equipped with an energy dispersive X-ray spectroscopy (EDX) system.

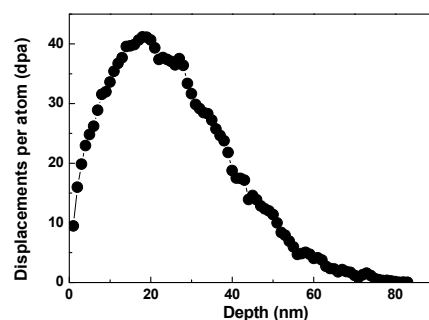


**Figure 1.** Depth profiles of the displacement damage (dpa) for the RAFM steel irradiated to a peak dose of 40 dpa with 100-keV Fe ions.

### 3. Results and Discussion

Figure 2 shows the unirradiated microstructure of a RAFM steel sample containing many pre-existing carbides with sizes of approximately 100–300 nm along the long axis in the matrix. A bright-field micrograph after 40 dpa of Fe ion irradiation at 300 °C is shown in Figure 3. A systematic selected-area electron diffraction (SAED) pattern of the pre-existing precipitates obtained from the unirradiated and irradiated specimens are shown in the upper right of the panels in Figures 2 and 3a, respectively. The calculated d-spacing of the (111), (200), (331), (422) and (511) spots were 0.6145 nm, 0.532 nm, 0.244 nm, 0.217 nm and 0.205 nm, respectively, which is parallel with the Pcpdfwin file (No. 781500) that originated from the  $M_{23}C_6$  consisting mainly of Cr and Fe. It should be noted that the  $(11\bar{1})$  and  $(200)$  reflections make a  $[011]$  zone axis (Figure 2), which paralleled the  $[0\bar{1}1]$  zone axis by  $(422)$ ,  $(1\bar{3}\bar{3})$  and  $(5\bar{1}\bar{1})$  reflections in Figure 3a.

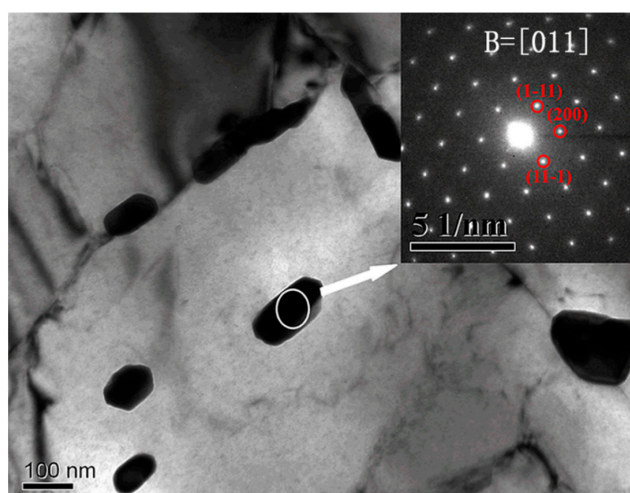


**Figure 2.** Bright-field micrograph of the unirradiated RAFM steel, in which many precipitates were located at the martensitic lath and grain boundaries. The microstructure of pre-existing precipitates was identified by the selected-area electron diffraction (SAED) patterns that are shown in the upper right of panels. The diffraction patterns indicate that it is a  $M_{23}C_6$  precipitate.

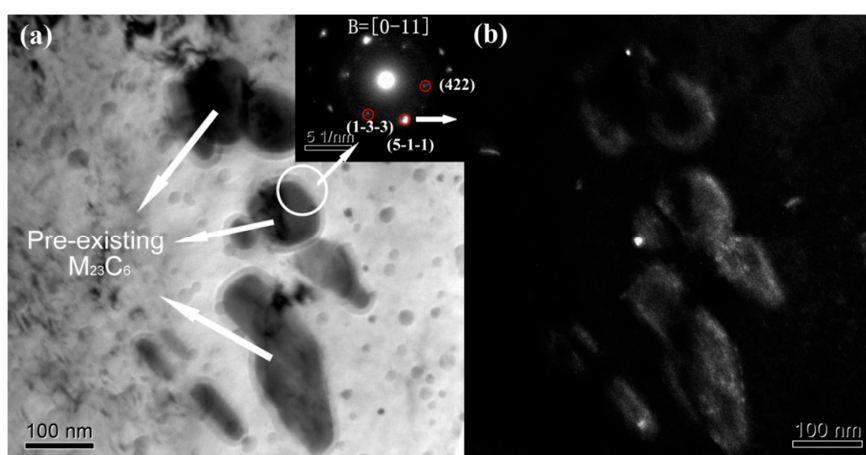


**Figure 3.** (a) Micrograph of the RAFM steel after 40 dpa Fe ion irradiation at 300 °C. An obvious change takes place at the periphery of the pre-existing precipitates. Simultaneously, a large number of small precipitates appear in the matrix; (b) is the dark-field image of (a), which is taken from the  $(5\bar{1}\bar{1})$  diffraction spot indicated by the white arrow.

Remarkable changes in the original pre-existing  $M_{23}C_6$  precipitates were found in the 40 dpa Fe ion irradiated specimen, which is shown in Figure 3a. The contrast at the periphery of the  $M_{23}C_6$  precipitates was reduced or weakened. A large number of new small phases appeared in parallel near the pre-existing  $M_{23}C_6$  precipitate after the irradiation. The original pre-existing  $M_{23}C_6$  precipitate periphery (the matrix/carbide interface) seemed to grow, with the width of the extended region being about 10–30 nm. In the right inset of Figure 3a, the SAED patterns show the amorphous diffraction halos accompanied by diffraction spots. The patterns contain three parts: the  $M_{23}C_6$  precipitate, matrix/carbide interface and the matrix, which is marked by a white circle. The  $(5\bar{1}1)$ ,  $(1\bar{3}3)$  and  $(422)$  diffraction spots originate from the  $M_{23}C_6$  precipitate as discussed above. The dark-field image of the  $M_{23}C_6$  precipitate shown in Figure 3b was from the  $(5\bar{1}1)$  diffraction spot marked by the white arrow. On the one hand, all the small phases were completely black in Figure 3b, which further indicated that the structure of the small new phase is not parallel to  $M_{23}C_6$ . On the other hand, Figure 3b shows that all  $M_{23}C_6$  carbides were bright and the peripheral region was brighter than the center of carbide. The electron transmittance in the periphery region was higher than that in the  $M_{23}C_6$  carbides. The appearance of diffraction halos indicated that the brighter periphery region (i.e., the matrix/carbide interface) is amorphous. From Figure 3, one can conclude that the pre-existing  $M_{23}C_6$  precipitate periphery was unstable under Fe ion irradiation. The loss of crystallinity of the  $M_{23}C_6$  particles also appeared in our previous studies [22,23]. The seemingly extended region indicates the dissolution of the pre-existing  $M_{23}C_6$  precipitates, which is similar to the heavy ion-irradiated or neutron-irradiated ferritic steels at 300–500 °C [24,25]. They also indicate that the pre-existing  $M_{23}C_6$  precipitates were partially dissolved after irradiation, especially at elevated irradiation temperatures. Kai et al. [24] also indicated that the modification of pre-existing  $M_{23}C_6$  precipitates due to 14-MeV Ni ion irradiation was very similar to the results of the thermal annealed ferritic steel. A vague explanation was given that irradiation would accelerate the thermal diffusion and in turn, enhance the thermal/aging effect, which is consistent with the mechanism of radiation-enhanced diffusion [26]. However, a more detailed reason for the dissolution of pre-existing  $M_{23}C_6$  should also be investigated from the view point of elemental segregation.

The compositions of the precipitate, peripheral amorphous region and matrix in the 40 dpa irradiated RAFM steel at 300 °C were investigated with STEM/EDX microanalysis (Figure 4). Fe, Cr, W and C were analyzed using EDX mapping, with no other elements having appeared in the spectra. The EDX spectra and the elemental compositions (in wt. %) of the different regions marked by white arrays (Figure 4a) are shown in Figure 4b–d. Compared to the chemical composition of the matrix (Figure 4d), the precipitate includes a greater content of C and Cr elements (Figure 4a). This also indicates that the precipitate is Cr-rich  $M_{23}C_6$ , which is consistent with the SAED result. The M mainly represents the Cr element and also contains Fe, W and other elements [16,27,28]. The EDX spectra collected from the interface between the precipitate and the matrix has a higher C amount. In addition, an elemental map was constructed in the same region as that in Figure 4a, while Figure 4e shows the High-Angle Annular Dark Field (HAADF) STEM images of the same precipitate. Figure 4f–i shows the EDX- $K\alpha$  mapping of Fe, Cr, W and C in the pre-existing precipitates after irradiation. The bright contrast in EDX elemental map represents a high elemental concentration. Therefore, Cr is mainly present in the precipitate. They also highlight the increased Fe and W contents in the pre-existing precipitates. However, considering the uneven thickness between the precipitates and the matrix (the precipitate region is thicker than that of the matrix in Figure 4), Fe and W elements should be distributed homogeneously. It should be noted that a high C element concentration appears at the interface between the precipitate and the matrix (i.e., the amorphous region). The reasons for this are not clear but one possibility is that the  $M_{23}C_6$  phases decompose during irradiation because of the loss of carbon atoms into the interface through irradiation-enhanced diffusion. The STEM/EDX map reveals a “Core/Shell” morphology for the  $M_{23}C_6$  precipitates after irradiation with 40 dpa Fe ions and a percolated structure of C-enrichment extending from the precipitate. It has a C-rich “Shell” and a Cr-rich “Core”, with C atoms segregated in the peripheral amorphous region. As discussed above,

the C-rich “Shell” region is brighter than the  $M_{23}C_6$  carbides in the dark-field image. The electron transmittance in the C-rich “Shell” region is higher than that in the precipitate and matrix. As presented in the literature, the irradiation increases the diffusion rates and sustains the point defect flux from the precipitate/matrix to the sinks (i.e., the interface between carbide and matrix). The defect concentration gradient near the interface makes the undersize atoms (i.e., C atoms) segregate to the sinks assisted by the formation of the solute–self-interstitial complexes [29]. The oversized Cr atoms become depleted along the interface between the  $M_{23}C_6$  precipitate and the matrix according to the solute-drag self-interstitial driven mechanisms [28–30]. Thus, the ion irradiation enhances the loss of crystallinity of the  $M_{23}C_6$  phase and decreases the size of the Cr-rich “core” through the irradiation-enhanced diffusion.

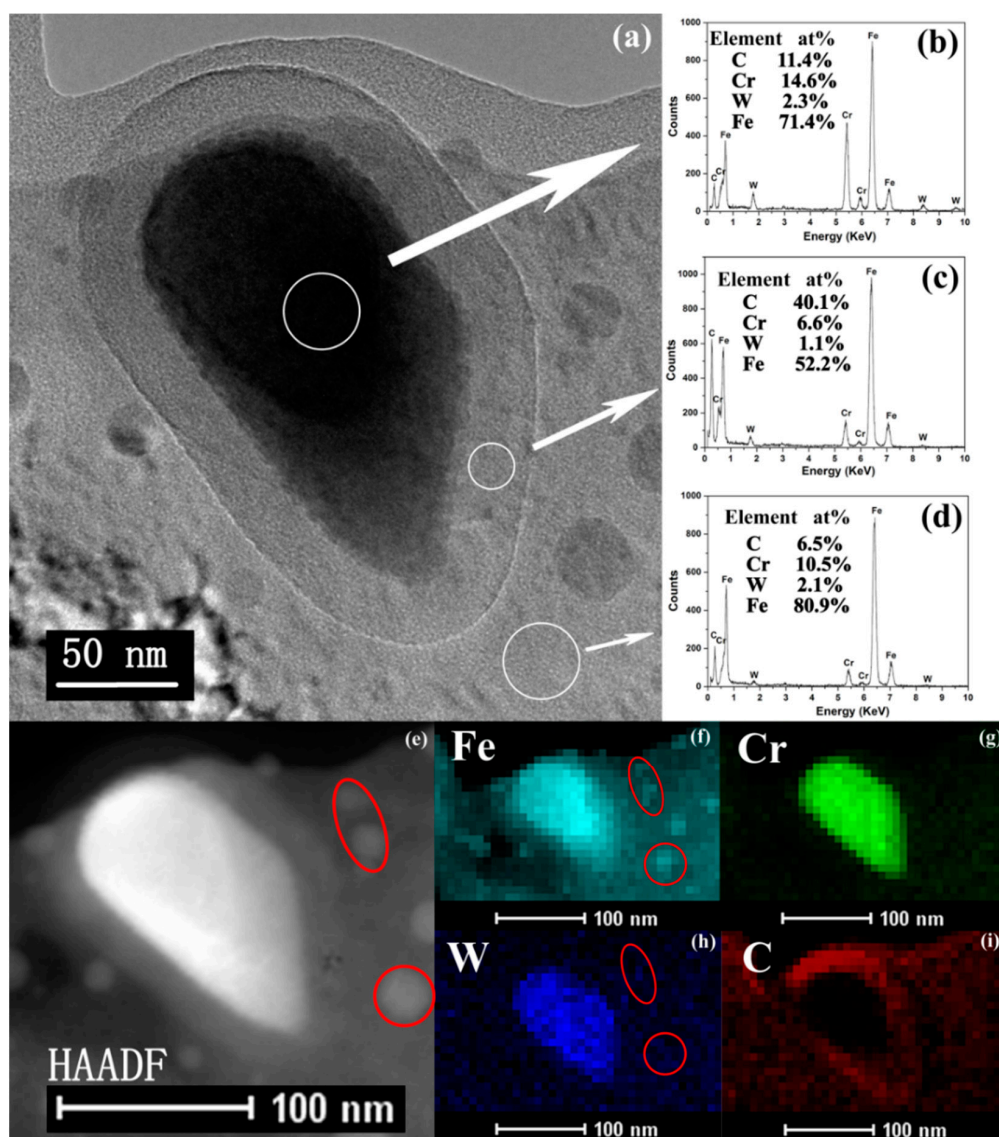


**Figure 4.** (a) Micrograph of the  $M_{23}C_6$  precipitates after Fe ion irradiation; (b–d) Chemical compositions in the different regions marked by the white arrows are analyzed by EDX; (b) EDX energy spectrum of the precipitate region; (c) EDX results at the matrix/carbide interface (amorphous region); (d) EDX spectrum of the matrix; (e) HAADF–STEM image and (f–i) corresponding EDX elemental mappings of Fe, Cr, W and C elements for the pre-existing  $M_{23}C_6$  precipitate and the new phase, respectively.

A large number of small new precipitates gathered around the pre-existing  $M_{23}C_6$  precipitate in Figure 5, which are not  $M_{23}C_6$  as indicated by Figure 3b. Thus, the EDX elemental maps were

also measured for the new phase (see Figure 4f–i). The Fe and W elements were enriched in the new small precipitates (see the red circles in Figure 4). Tanigawa et al. [31] predicted the possibility of the formation of  $M_6C$  in the F82H steel after irradiation at 300 °C, but no detailed microstructure examination was performed. In order to clarify the structure of the new phase, a high-resolution TEM (HRTEM) image of the small precipitate was obtained as shown in Figure 5b. The calculated d-spacing of the (220) and (422) diffraction spots were 0.226 nm and 0.401 nm, respectively (Pcpdwin file No. 781990). This confirms that the small precipitate has the  $M_6C$  (i.e.,  $Fe_3W_3C$ ) structure. Irradiation can increase the diffusion rates through the production of point defects, which can be trapped by the interface between  $M_{23}C_6$  precipitates and matrices. In-situ observations revealed that the small  $M_{23}C_6$  fragment can separate from the pre-existing  $M_{23}C_6$  precipitates in 2-MV electron irradiated F82H steel [32]. The irradiation-induced phase transformations are possible because the free energies of the different phases are changed by the excess energy introduced into the lattice. The carbide transformations of  $M_{23}C_6$  to  $M_6C$  have been observed at 700 °C by Inoue et al. [33], which was determined based on the following relationships of crystal orientations between  $M_{23}C_6$  and  $M_6C$ :  $(\bar{1}10) M_{23}C_6 // (\bar{1}10) M_6C$ ,  $(\bar{1}11) M_{23}C_6 // (11\bar{1}) M_6C$ , and  $(112) M_{23}C_6 // (112) M_6C$ . Therefore, the formation of a new  $M_6C$  phase near the pre-existing  $M_{23}C_6$  precipitate may be transformed from a small  $M_{23}C_6$  fragment separated from the pre-existing precipitates, with irradiation at elevated temperature promoting these processes. As discussed above, the  $M_{23}C_6$  carbides can prevent sliding of the grain boundary [8] and strengthen the mechanical properties of the RAFM steels [6]. The dissolution of the pre-existing  $M_{23}C_6$  carbides was detrimental to the mechanical properties, especially the ductile-to-brittle transition temperature [34]. Simultaneously, the high energy precipitate–matrix interfaces due to Cr and C segregation favored fracture paths [5]. The precipitation of  $M_6C$  caused a reduction in material toughness [35]. Thus, the phase transformation ( $M_{23}C_6 \rightarrow M_6C$ ) resulted in degraded mechanical properties, especially the ductile-to-brittle transition temperature. The effect of the  $M_{23}C_6$  dissolution and re-precipitation of  $M_6C$  on the fracture toughness requires further research. Ghidelli et al. [21] suggested a possible approach to study the micro-scale fracture toughness by obtaining pillar splitting measurements.

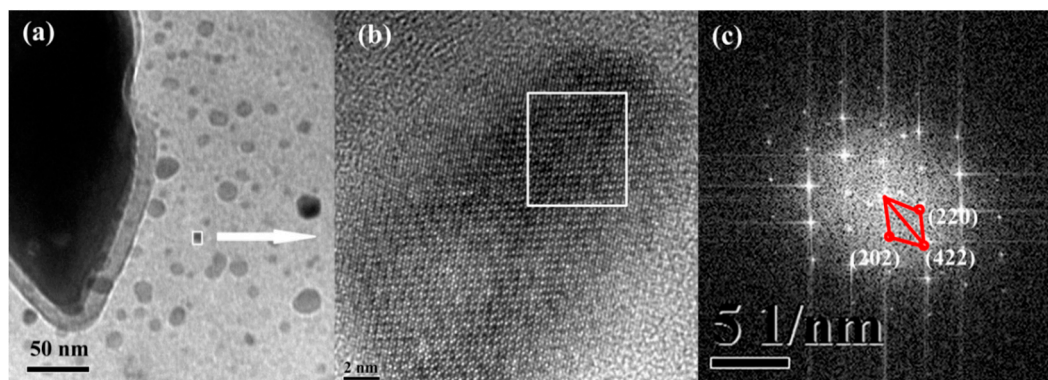


**Figure 5.** (a) TEM micrograph of the small precipitates in the matrix of RAFM steel irradiated with 40 dpa Fe ion at 300 °C; (b) Corresponding HRTEM image of the small precipitate; and (c) Fast Fourier transformation (FFT) pattern of the white square region in (b).

#### 4. Conclusions

In the present work, we investigated the instability of  $M_{23}C_6$  precipitates in ion-damaged RAFM steel via STEM/EDX. A “Core/Shell” structure (C-rich “Shell” and Cr-rich “Core”) was formed in the pre-existing  $M_{23}C_6$  precipitates after the irradiation with 40 dpa Fe ion at 300 °C. The SAED measurements combined with the bright/dark-field contrast images showed that the extended C-rich “Shell” was amorphous with carbon atoms percolated into the interface. Ion irradiation actually enhances the loss of crystallinity of the  $M_{23}C_6$  phase and decreases the size of the Cr-rich “Core”

through irradiation-enhanced diffusion. The small new phase gathering around the pre-existing  $M_{23}C_6$  precipitate has a  $M_6C$  ( $Fe_3W_3C$ ) structure, which was confirmed by SAED and EDX analyses. The irradiation at elevated temperatures promoted the separation of small  $M_{23}C_6$  fragments from the pre-existing precipitates and transformation into a new  $M_6C$  phase.

**Author Contributions:** Z.Y., S.J. and L.G. conceived and designed the experiments; W.Z. and L.Y. performed the experiments; S.J. and L.S. analyzed the data; Z.Y. and S.J. wrote the paper.

**Funding:** This research was funded by the [National Natural Science Foundation of China] grant number [11505192, 11775162 and 11775236].

**Conflicts of Interest:** The authors declare no conflict of interest.

## References

1. Huang, Q.Y. Status and improvement of CLAM for nuclear application. *Nucl. Fusion* **2017**, *57*, 086042. [[CrossRef](#)]
2. Yu, J.N.; Huang, Q.Y.; Wan, F.R. Research and development on the China low activation martensitic steel (CLAM). *J. Nucl. Mater.* **2007**, *367*, 97–101. [[CrossRef](#)]
3. Yin, F.S.; Jung, W.S.; Chung, S.H. Microstructure and creep rupture characteristics of an ultra-low carbon ferritic/martensitic heat-resistant steel. *Scr. Mater.* **2007**, *57*, 469–472. [[CrossRef](#)]
4. Li, Q.S.; Shen, Y.Z.; Zhu, J.; Huang, X.; Shang, Z.X. Evaluation of Irradiation Hardening of P92 Steel under Ar Ion Irradiation. *Metals* **2018**, *8*, 94. [[CrossRef](#)]
5. Di Martino, S.F.; Riddle, N.B.; Faulkner, R.G. Controlling the ductile to brittle transition in Fe-9%Cr ODS steels. *J. Nucl. Mater.* **2013**, *442*, S124–S132. [[CrossRef](#)]
6. Yan, B.Y.; Liu, Y.C.; Wang, Z.J.; Liu, C.X.; Si, Y.H.; Li, H.J.; Yu, J.X. The Effect of Precipitate Evolution on Austenite Grain Growth in RAFM Steel. *Materials* **2017**, *10*, 1017. [[CrossRef](#)] [[PubMed](#)]
7. Xiao, X.; Liu, G.Q.; Hu, B.F.; Wang, J.S.; Ma, W.B. Microstructure Stability of V and Ta Microalloyed 12%Cr Reduced Activation Ferrite/Martensite Steel during Long-term Aging at 650 °C. *J. Mater. Sci. Technol.* **2015**, *31*, 311–319. [[CrossRef](#)]
8. Duan, Z.X.; Pei, W.; Gong, X.B.; Chen, H. Superplasticity of Annealed H13 Steel. *Materials* **2017**, *10*, 870. [[CrossRef](#)] [[PubMed](#)]
9. Shen, T.L.; Wang, Z.G.; Yao, C.F.; Sun, J.R.; Li, Y.F.; Wei, K.F.; Zhu, Y.B.; Pang, L.L.; Cui, M.H.; Wang, J.; et al. The sink effect of the second-phase particle on the cavity swelling in RAFM steel under Ar-ion irradiation at 773 K. *Nucl. Instrum. Methods Phys. Res. Sect. B* **2013**, *307*, 512–515. [[CrossRef](#)]
10. Tan, L.; Katoh, Y.; Snead, L.L. Stability of the strengthening nanoprecipitates in reduced activation ferritic steels under  $Fe^{2+}$  ion irradiation. *J. Nucl. Mater.* **2014**, *445*, 104–110. [[CrossRef](#)]
11. Tanigawa, H.; Sakasegawa, H.; Ogiwara, H.; Kishimoto, H.; Kohyama, A. Radiation induced phase instability of precipitates in reduced-activation ferritic/martensitic steels. *J. Nucl. Mater.* **2007**, *367*, 132–136. [[CrossRef](#)]
12. Dong, Q.S.; Yao, Z.W.; Wang, Q.; Yu, H.B.; Kirk, M.A.; Daymond, M.R. Precipitate Stability in a Zr-2.5Nb-0.5Cu Alloy under Heavy Ion Irradiation. *Metals* **2017**, *7*, 287. [[CrossRef](#)]
13. Rowcliffe, A.F.; Lee, E.H. High-Temperature Radiation-Damage Phenomena in Complex Alloys. *J. Nucl. Mater.* **1982**, *108*, 306–318. [[CrossRef](#)]
14. Zhang, C.H.; Chen, K.Q.; Wang, Y.S.; Sun, J.G.; Hu, B.F.; Jin, Y.F.; Hou, M.D.; Liu, C.L.; Sun, Y.M.; Han, J.; et al. Microstructural changes in a low-activation Fe-Cr-Mn alloy irradiated with 92 MeV Ar ions at 450 °C. *J. Nucl. Mater.* **2000**, *283*, 259–262. [[CrossRef](#)]
15. Klueh, R.L.; Alexander, D.J.; Rieth, M. The effect of tantalum on the mechanical properties of a 9Cr-2W-0.25V-0.07Ta-0.1C steel. *J. Nucl. Mater.* **1999**, *273*, 146–154. [[CrossRef](#)]
16. Zhao, M.Z.; Liu, P.P.; Zhu, Y.M.; Wan, F.R.; He, Z.B.; Zhan, Q. Effects of hydrogen isotopes in the irradiation damage of CLAM steel. *J. Nucl. Mater.* **2015**, *466*, 491–495. [[CrossRef](#)]
17. Dai, Y.; Bauer, G.S.; Carsughi, F.; Ullmaier, H.; Maloy, S.A.; Sommer, W.F. Microstructure in Martensitic Steel DIN 1.4926 after 800 MeV proton irradiation. *J. Nucl. Mater.* **1999**, *265*, 203–207. [[CrossRef](#)]
18. Dai, Y.; Carsughi, F.; Sommer, W.F.; Bauer, G.S.; Ullmaier, H. Tensile properties and microstructure of martensitic steel DIN 1.4926 after 800 MeV proton irradiation. *J. Nucl. Mater.* **2000**, *276*, 289–294. [[CrossRef](#)]

19. Dai, Y.; Maloy, S.A.; Bauer, G.S.; Sommer, W.F. Mechanical properties and microstructure in low-activation martensitic steels F82H and Optimax after 800-MeV proton irradiation. *J. Nucl. Mater.* **2000**, *283*, 513–517. [[CrossRef](#)]
20. Sencer, B.H.; Garner, F.A.; Gelles, D.S.; Bond, G.M.; Maloy, S.A. Structural evolution in modified 9Cr-1Mo ferritic/martensitic steel irradiated with mixed high-energy proton and neutron spectra at low temperatures. *J. Nucl. Mater.* **2002**, *307*, 266–271. [[CrossRef](#)]
21. Ghidelli, M.; Sebastiani, M.; Johanns, K.E.; Pharr, G.M. Effects of indenter angle on micro-scale fracture toughness measurement by pillar splitting. *J. Am. Ceram. Soc.* **2017**, *100*, 5731–5738. [[CrossRef](#)]
22. Jin, S.X.; Guo, L.P.; Yang, Z.; Fu, D.J.; Liu, C.S.; Tang, R.; Liu, F.H.; Qiao, Y.X.; Zhang, H.D. Microstructural evolution of P92 ferritic/martensitic steel under argon ion irradiation. *Mater. Charact.* **2011**, *62*, 136–142. [[CrossRef](#)]
23. Jin, S.X.; Guo, L.P.; Li, T.C.; Chen, J.H.; Yang, Z.; Luo, F.F.; Tang, R.; Qiao, Y.X.; Liu, F.H. Microstructural evolution of P92 ferritic/martensitic steel under Ar<sup>+</sup> ion irradiation at elevated temperature. *Mater. Charact.* **2012**, *68*, 63–70. [[CrossRef](#)]
24. Kai, J.J.; Kulcinski, G.L. 14 MeV nickel-ion irradiated HT-9 ferritic steel with and without helium pre-implantation. *J. Nucl. Mater.* **1990**, *175*, 227–236. [[CrossRef](#)]
25. Maziasz, P.J.; Klueh, R.L.; Vitek, J.M. Helium Effects on Void Formation in 9Cr-1MoVNB and 12Cr-1MoVW Irradiated in HFIR. *J. Nucl. Mater.* **1986**, *141*, 929–937. [[CrossRef](#)]
26. Chen, J.H.; Guo, L.P.; Liu, C.X.; Luo, F.F.; Li, T.C.; Zheng, Z.C.; Jin, S.X.; Yang, Z. Enhancement of room temperature ferromagnetism in Mn-implanted Si by He implantation. *Appl. Phys. Lett.* **2012**, *101*, 132413. [[CrossRef](#)]
27. Fang, C.M.; van Huis, M.A.; Sluiter, M.H.F. Formation, structure and magnetism of the  $\gamma$ -(Fe,M)<sub>23</sub>C<sub>6</sub> (M = Cr, Ni) phases: A first-principles study. *Acta Mater.* **2016**, *103*, 273–279. [[CrossRef](#)]
28. Klimiankou, M.; Lindau, R.; Moslang, A. Direct correlation between morphology of (Fe,Cr)<sub>23</sub>C<sub>6</sub> precipitates and impact behavior of ODS steels. *J. Nucl. Mater.* **2007**, *367*, 173–178. [[CrossRef](#)]
29. Lu, Z.; Faulkner, R.G.; Was, G.; Wirth, B.D. Irradiation-induced grain boundary chromium microchemistry in high alloy ferritic steels. *Scr. Mater.* **2008**, *58*, 878–881. [[CrossRef](#)]
30. Jiang, Z.H.; Feng, H.; Li, H.B.; Zhu, H.C.; Zhang, S.C.; Zhang, B.B.; Han, Y.; Zhang, T.; Xu, D.K. Relationship between Microstructure and Corrosion Behavior of Martensitic High Nitrogen Stainless Steel 30Cr15Mo1N at Different Austenitizing Temperatures. *Materials* **2017**, *10*, 861. [[CrossRef](#)] [[PubMed](#)]
31. Tanigawa, H.; Sakasegawa, H.; Klueh, R.L. Irradiation effects on precipitation in reduced-activation ferritic/martensitic steels. *Mater. Trans.* **2005**, *46*, 469–474. [[CrossRef](#)]
32. Kano, S.; Yang, F.; Shen, J.; Zhao, Z.; McGrady, J.; Hamaguchi, D.; Ando, M.; Tanigawa, H.; Hiroaki, A. Investigation of instability of M<sub>23</sub>C<sub>6</sub> particles in F82H steel under electron and ion irradiation conditions. *J. Nucl. Mater.* **2018**, *502*, 263–269. [[CrossRef](#)]
33. Inoue, A.; Masumoto, T. Carbide Reactions (M<sub>3</sub>C-M<sub>7</sub>C<sub>3</sub>-M<sub>23</sub>C<sub>6</sub>-M<sub>6</sub>C) during Tempering of Rapidly Solidified High-Carbon Cr-W and Cr-Mo Steels. *Metall. Trans. A* **1980**, *11*, 739–747. [[CrossRef](#)]
34. Wang, W.; Mao, X.D.; Liu, S.J.; Xu, G.; Wang, B. Microstructure evolution and toughness degeneration of 9Cr martensitic steel after aging at 550 A degrees C for 20000 h. *J. Mater. Sci.* **2018**, *53*, 4574–4581. [[CrossRef](#)]
35. Shiba, K.; Tanigawa, H.; Hirose, T.; Sakasegawa, H.; Jitsukawa, S. Long-term properties of reduced activation ferritic/martensitic steels for fusion reactor blanket system. *Fusion Eng. Des.* **2011**, *86*, 2895–2899. [[CrossRef](#)]

